

LA-UR-18-20960 (Accepted Manuscript)

Radiation resistance of oxide dispersion strengthened alloys: Perspectives from in situ observations and rate theory calculations

Liu, X.
Miao, Y.
Li, M.
Kirk, M.
Zhang, G.
Ukai, S.
Maloy, Stuart Andrew
Stubbins, J.

Provided by the author(s) and the Los Alamos National Laboratory (2018-07-03).

To be published in: Scripta Materialia

DOI to publisher's version: 10.1016/j.scriptamat.2018.01.018

Permalink to record: <http://permalink.lanl.gov/object/view?what=info:lanl-repo/lareport/LA-UR-18-20960>

Disclaimer:

Approved for public release. Los Alamos National Laboratory, an affirmative action/equal opportunity employer, is operated by the Los Alamos National Security, LLC for the National Nuclear Security Administration of the U.S. Department of Energy under contract DE-AC52-06NA25396. Los Alamos National Laboratory strongly supports academic freedom and a researcher's right to publish; as an institution, however, the Laboratory does not endorse the viewpoint of a publication or guarantee its technical correctness.

Radiation resistance of oxide dispersion strengthened alloys: perspectives from in situ observations and rate theory calculations

Xiang Liu^a, Yinbin Miao^b, Meimei Li^b, Marquis A. Kirk^b, Guangming Zhang^c, Shigeharu Ukai^d, Stuart A. Maloy^e, James F. Stubbins^{a,f}

^a*Department of Nuclear, Plasma, and Radiological Engineering, University of Illinois at Urbana-Champaign, Urbana, IL 61801, USA*

^b*Nuclear Engineering Division, Argonne National Laboratory, Lemont, IL 60439, USA*

^c*Qingdao University of Technology, Qingdao, Shandong 266033, China*

^d*Materials Science and Engineering, Faculty of Engineering, Hokkaido University, N13, W-8, Kita-ku, Sapporo, Hokkaido, 060-8628, Japan*

^e*Materials Science and Technology Division, Los Alamos National Laboratory, Los Alamos, NM 87545, USA*

^f*International Institute for Carbon Neutral Energy Research (WPI-I2CNER), Kyushu University, 744 Motoooka, Nishi-ku, Fukuoka 819-0395, Japan*

Abstract

Here, in situ ion irradiation was employed to observe the buildup of radiation damage of a ferritic/martensitic oxide dispersion strengthened alloy. The radiation resistance of this alloy is manifested by the much more stable dislocation structure compared to the rapid buildup of black-dot dislocation loops, loop growth, and formation of network dislocations in a conventional ferritic/martensitic alloy under the same irradiation conditions. The difference lies in the ultra-stable, high-density dispersoids known as Y-Ti-O nanoparticles. Rate theory calculations indicate that the nanoparticles significantly reduce the concentration of freely migrating defects and suppress radiation-enhanced diffusion, leading to superior radiation resistance.

Keywords: Oxide dispersion strengthened (ODS) alloy; Dislocation structure; Microstructure; Transmission electron microscopy; Radiation enhanced diffusion (RED).

Advanced nuclear reactor systems with inherent safety features are being developed as reliable and sustainable clean energy sources. However, the harsh reactor environment, especially high-dose neutron irradiation (>100 dpa), rules out the extended use of most conventional structural materials. By introducing ultra-stable, high-density ($\sim 10^{23}$ n/m³) dispersoids to suppress irradiation-induced defect formation, nanostructured oxide dispersion strengthened (ODS) alloys represents one of the most promising candidate materials for structural applications in advanced reactors [1]. Commonly used dispersoids are Y-Ti-O nanoparticles (2–4 nm) in ODS Fe-Cr alloys and relatively coarse (~ 10 nm) Y-Al-O nanoparticles in ODS FeCrAl alloys [2–4]. The stability of these nanoparticles under irradiation and high temperature heat treatment has been demonstrated by several studies [5–12].

A previous review paper [1] compared the helium bubbles in ODS alloy MA957 versus the bubbles in reduced-activation martensitic alloys Eurofer97 and F82H, and found that the helium bubbles in irradiated ODS alloys tend to have higher number density and smaller size, which was also confirmed by a recent study [13]. It is suggested that the nanoparticles in ODS alloys help absorbing helium atoms and protect the grain boundary from helium embrittlement. These findings provide some idea about the enhanced

radiation resistance of ODS alloys. However, most existing studies rely on the ex situ irradiation data and often the comparisons could only be made on alloys with distinct chemical composition, heat treatment, and/or initial microstructure. Moreover, to the best of our knowledge, few data on the evolution of the dislocation structure, which is closely related to irradiation hardening, of ODS alloys versus non-ODS alloys under similar irradiation conditions can be found in literature.

To compare the radiation response, especially the evolution of the dislocation structure, of ODS alloys versus the non-ODS versions, this study employed in situ transmission electron microscopy (TEM) with concurrent ion irradiation so that a direct comparison of the microstructure changes in various alloy systems under the same exposure conditions is possible. The in situ capability allows the dynamic observation of the microstructure evolution of exactly the same area over a range of dose levels. In this study, the comparison was made between a Fe-9Cr ODS ferritic/martensitic (F/M) alloy (designated 9CrODS) and a Fe-9Cr F/M alloy, T91. The 9Cr alloys belong to the high Cr alloy family that show promising resistance to void swelling and irradiation creep [14]. Table 1 shows the nominal chemical composition of the as-received materials.

Table 1. Nominal chemical composition of as-received T91 and 9CrODS alloys, in wt.%.

Alloy	Fe	Cr	C	Si	Mn	Ni	W	N	Mo	Nb	Ti	Y	O	Y ₂ O ₃
T91	Bal.	9.24	0.089	0.28	0.47	0.16	-	0.035	0.96	0.054	0.002	-	0.008	-
9CrODS	Bal.	9.08	0.14	0.06	0.09	0.03	1.97	0.013	-	-	0.23	0.29	0.16	0.37

The as-received T91 and 9CrODS underwent similar heat treatment: T91 was normalized at 1037 °C for 1 h, air cooled, and then tempered at 760 °C for 1 h and air cooled, and 9CrODS was normalized at 1050 °C for 1 h, air cooled, followed by tempering at 800 °C for 1 h and air cooled.

The in situ ion irradiation experiments were performed at the IVEM-Tandem facility, Argonne National Laboratory (ANL). The experimental setup was identical to the one previously described by Liu *et al.* [15]. A Hitachi 9000 NAR electron microscope operated at 200 kV was used for post-irradiation TEM imaging. The incident ion beam was 30° to the electron beam and on average ~ 15° to the foil normal. TEM thin foils were irradiated by 1 MeV Kr⁺⁺ ions at 400 °C up to 4.2×10^{15} ions/cm², corresponding to 7.0 dpa under the Kinchin-Pease option using SRIM calculation with displacement energy set to 40 eV [16,17]. The ion flux was kept at 6.25×10^{11} ions/(cm²·s), representing a dose rate of 1.0×10^{-3} dpa/s in the thin foil region and the Kr⁺⁺ ions were sufficiently energetic to pass through the foil.

In order to make the comparison more reliable, martensite grains with similar initial line dislocation density ($\sim 1 \times 10^{14}$ m⁻²) in 9CrODS and T91 were chosen, and the TEM images were taken under similar kinematic diffraction conditions with g_{110} strongly excited. Fig. 1 shows the in situ TEM observations of the microstructure evolution of 9CrODS versus F/M steel T91. The results of T91 were previously described in detail by Liu *et al.* [15]. As can be seen from Fig. 1 (a)–(e), the dislocation structure in 9CrODS is very stable even after being irradiated to 4.2×10^{15} ions/cm² (~ 7 dpa), as manifested by very low-density black-dot damage accumulation. Both the dislocation loops and the Y-Ti-O nanoparticles can appear as dark spots in the bright-field images, but the dislocation loops are distinguishable from the nanoparticles as they appear as bright spots in the corresponding weak-beam dark-field images. One example of this imaging effect can be found in the Supplementary Material. In Fig. 1, several possible black-dot loops were marked by red arrows. The loops remained small black-dots (2–4 nm) and no loop growth was observed up to 7 dpa. Some changes did occur to the pre-existing dislocations, due to dislocation-defect interactions. In addition to the negligible amount of dislocation loops, post-irradiation examination (PIE) also did not find any resolvable voids.

In contrast, as shown in Figs. 1 (f)–(j), T91 maintained relative stability only up to around 6.0×10^{14} ions/cm² (~ 1 dpa), and black-dot dislocation loops started to accumulate around 1.8×10^{15} ions/cm² (~ 3 dpa). The black-dot dislocation loops increased in size with increasing dose. One example of loop growth is the loop marked by red circle in Figs. 1 (i) and (j). Loops of 10–20 nm were commonly found after the sample was irradiated to 4.2×10^{15} ions/cm². In addition to the buildup of black-dot loops and loop growth, apparent dislocation segments also occurred around 3.0×10^{15} ions/cm² (~ 5 dpa). It is known that in F/M steels, the dislocation segments will evolve into network dislocations, which contribute to irradiation hardening by impeding dislocation motion as well as void swelling by preferentially absorbing interstitials (sink bias) in the high dose regime.

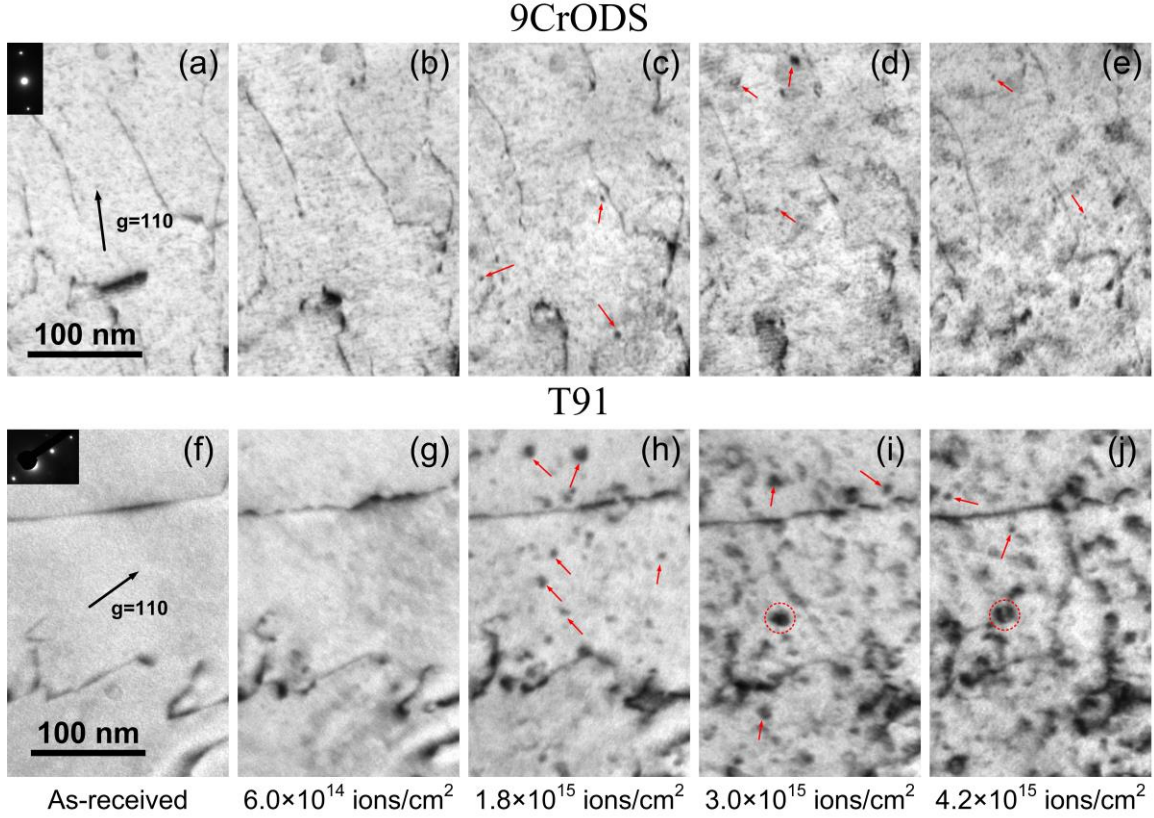


Fig. 1. In situ TEM observations of the microstructure evolution of (a)–(e) 9CrODS, and (f)–(j) F/M steel T91 at various dose levels. Both specimens were irradiated by 1.0 MeV Kr⁺⁺ ions at 400 °C. The T91 result is from previous work [15].

In order to understand the noticeable difference in dislocation structure evolution of 9CrODS versus T91, rate theory calculations were performed using the chemical rate equation [18]:

$$\frac{\partial C_j}{\partial t} = \epsilon_{FM} K_0 - K_{iv} C_i C_v - K_{js} C_j C_s, \quad (1)$$

where $j=i$ or v , ϵ_{FM} is the production efficiency of freely migrating defects (fmd), K_0 is the dpa rate, K is the rate constant for the reaction indicated by the subscripts, C_i , C_v , and C_s are the concentrations of interstitials, vacancies, and sinks, respectively. For F/M steels such as T91, the sinks are pre-existing dislocations and grain boundaries, and Eq. (1) can be written as [18–20]:

$$\frac{\partial C_j}{\partial t} = \epsilon_{FM} K_0 - \frac{4\pi r_{iv}}{\Omega} (D_i + D_v) C_i C_v - \frac{2\pi D_j}{\ln(\mathcal{R}/R_{jd})} C_j \rho_d - \frac{3\pi^2}{L^2} D_j C_j, \quad (2)$$

where ρ_d is the dislocation density, r_{iv} is the defect recombination radius, L is the grain size, \mathcal{R} is defined by $\pi\mathcal{R}^2\rho_d = 1$, R_{jd} is the capture radius for defect j , and D_j is the diffusion coefficient. For ODS alloy, an additional term accounting for the high-density nanoparticles needs to be included:

$$\frac{\partial C_j}{\partial t} = \epsilon_{FM} K_0 - \frac{4\pi r_{iv}}{\Omega} (D_i + D_v) C_i C_v - \frac{2\pi D_j}{\ln(\mathcal{R}/R_{jd})} C_j \rho_d - \frac{3\pi^2}{L^2} D_j C_j - 4\pi r_p D_j C_j \rho_p, \quad (3)$$

where r_p is the nanoparticle-defect capture radius, ρ_p is the number density of the nanoparticles.

For radiation-enhanced diffusion (RED), only considering the contributions from point defects [19]:

$$D_{rad} = f_v D_v C_v + f_i D_i C_i, \quad (4)$$

where f_j is the jump correlation coefficient of defect j ($j=i$ or v).

Table 2 lists the input parameters for rate theory calculations. The parameters are from recent work on modeling radiation-induced segregation (RIS) in F/M alloys [21] and previous rate theory studies [18–20,22,23].

Table 2. Input parameters for rate theory calculations.

Parameter	Value
find production efficiency, ϵ_{FM}	0.04 [19]
vacancy jump correlation factor, f_v	0.727 [19,21]
interstitial jump correlation factor, f_i	0.727 [19,21]
vacancy Debye frequency, ν_v	$1.5 \times 10^{13} \text{ s}^{-1}$ [21]
interstitial Debye frequency, ν_i	$1.5 \times 10^{12} \text{ s}^{-1}$ [21]
vacancy formation energy of Cr, E_{fv}^{Cr}	2.25 eV [21]
vacancy migration energy of Cr, E_{mv}^{Cr}	0.55 eV [21]
vacancy formation energy of Fe, E_{fv}^{Fe}	1.6 eV [21]
vacancy migration energy of Fe, E_{mv}^{Fe}	0.63 eV [21]
interstitial migration energy of Cr, E_{mi}^{Cr}	0.28 eV [21]
interstitial migration energy of Fe, E_{mi}^{Fe}	0.35 eV [21]
lattice constant, a	0.288 nm [24]
Burgers vector, b	0.249 nm [24]
atomic volume, Ω	0.012 nm^3 [23]
recombination volume, $\frac{4}{3}\pi r_{iv}^3$	100 Ω [18]
dislocation density, ρ_d	10^{14} m^{-2} [15]
dislocation-vacancy capture radius, R_{vd}	$4b$ [22]
dislocation-interstitial capture radius, R_{id}	$10b$ [22]
nanoparticle number density, ρ_p	10^{23} m^{-3}
nanoparticle defect capture radius, r_p	2.0 nm

Fig. 2 shows the calculated radiation enhanced diffusivity D_{rad} for four cases: (1) recombination only ($C_s \approx 0$), (2) sink 1: recombination with dislocation and grain boundary sinks only, (3) sink 2: recombination with nanoparticle sinks only, and (4) sink 3: recombination with dislocation, GB, and nanoparticle sinks. The chosen parameters such as dislocation density, grain size, nanoparticle size and number density are consistent with commonly reported values in F/M steels and ODS steels. As reference, the thermally-activated diffusivity D_{th} is also plotted in Fig. 2.

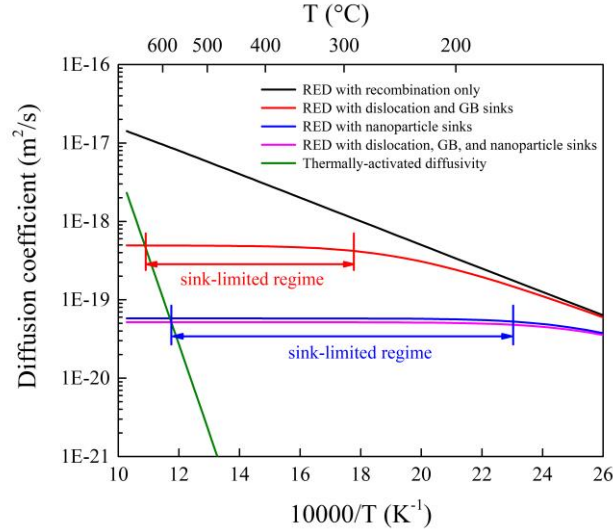


Fig. 2. Calculated diffusion coefficient for thermally-activated diffusion and radiation-enhanced diffusion with various sinks.

As can be seen from Fig. 2, the D_{rad} for recombination only follows Arrhenius behavior with an activation energy of half of the vacancy migration energy E_{mv} . The D_{rad} in black well represents most solution annealed Fe-Cr model alloys that have coarse grains and low dislocation densities ($\sim 10^{11} \text{ m}^{-2}$). The introduction of dislocations and GBs into the material effectively reduces the D_{rad} and the sink-limited regime lies in the $\sim 290 \text{ }^\circ\text{C}$ to $630 \text{ }^\circ\text{C}$ range, as shown in the red curve. This represents the case for most ferritic/martensitic steels that have high dislocation density and small grain size. In comparison, the nanoparticle sinks are much more efficient in suppressing D_{rad} , as the D_{rad} in blue is about one order of magnitude lower than the D_{rad} in red at temperatures where RED dominates. The temperature range of the sink-limited regime is also lowered to $\sim 150 \text{ }^\circ\text{C}$ to $560 \text{ }^\circ\text{C}$. For ODS steels, the nanoparticles play the dominant role in suppressing RED, as further including the dislocations and GBs sinks only helps slightly in suppressing RED (the D_{rad} in pink is only slightly lower than the D_{rad} in blue).

Further comparison can be made for the concentration of freely migrating defects (fmd). The dislocation-vacancy and dislocation-interstitial capture radii in Table 2 are different, which is known as the sink bias. Fig. 3 shows the calculated relative defect concentration (absolute concentration divided by the concentration of the recombination only case). The vacancy/interstitial concentrations are named by their subscripts: v represents vacancy and i represents interstitial, r is the recombination only ($C_s \approx 0$) case, aforementioned sink 1, 2, 3 cases are denoted by s1, s2, s3, respectively.

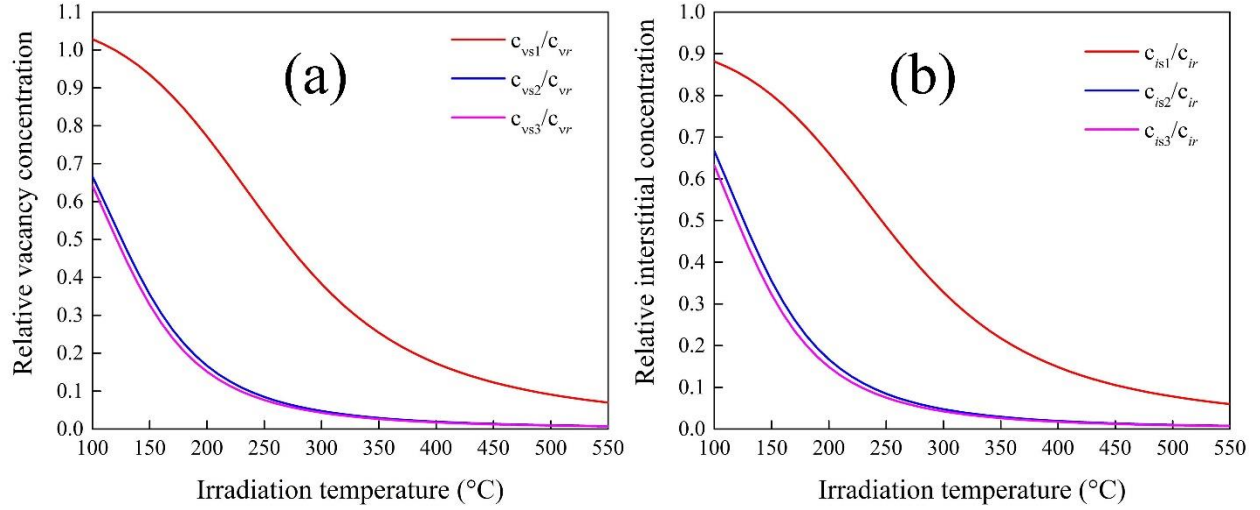


Fig. 3. Calculated relative (a) vacancy concentration and (b) interstitial concentration for sink 1: dislocations and GBs, sink 2: nanoparticles, and sink 3: nanoparticles, dislocations, and GBs. The concentrations are normalized by the recombination-only ($C_s \approx 0$) defect concentrations.

As can be seen from Fig. 3, the fmd concentrations of s2 and s3 cases are significantly lower than the s1 case. Table 3 lists the vacancy and interstitial concentrations (in atomic fraction) for different sinks at 400 °C, the irradiation temperature for T91 and 9CrODS. For sink 1, C_{is1}/C_{ir} is 0.0145, whereas C_{vs1}/C_{vr} is about 0.0176. The 21% difference is due to the sink bias of dislocations ($B \approx 0.29$). For sink 2, both C_{is2}/C_{ir} and C_{vs2}/C_{vr} are about 0.0019. For sink 3, C_{is3}/C_{ir} is 0.00168 and C_{vs3}/C_{vr} is 0.00176. F/M steel T91 and 9CrODS steel can be regarded approximately as belonging to sink 1 and sink 3 case, respectively. These results show that the nanoparticles in ODS steels are much more efficient in absorbing point defects and suppressing the buildup of defect clusters. In contrast, the dislocations and GBs at the calculated density level play a less important role in terms of point defect annihilation.

Table 3. Calculated vacancy and interstitial concentrations (in atomic fraction) for different sinks at 400 °C.

	C_i	C_v
$C_s \approx 0$	2.2E-9	6.8E-8
sink 1	3.2E-10	1.2E-8
sink 2	4.2E-11	1.3E-9
sink 3	3.7E-11	1.2E-9

The aforementioned results assume a constant dislocation density and did not take into account the buildup of defect clusters at different dose levels. The exact solution of the surviving fmds and RED requires coupled defect balance equations that can model the evolution of defect clusters. However, the coupling of dose-dependent defect clusters and dislocation densities should not change our order-of-magnitude analysis. As a simple estimation of the influence of dislocation density on the radiation-enhanced diffusion coefficient for sink 1, calculations were made at three different dislocation densities and the results can be found in the Supplementary Material. For T91 irradiated at 400 °C up to 7 dpa, the defect concentrations may be smaller by a factor of 2 than the ones for sink 1 in Table 3.

In summary, the superior radiation stability of a 9CrODS steel is demonstrated through the direct comparison with a 9Cr F/M steel T91 using in situ TEM heavy ion irradiation. In contrast to various

changes such as rapid buildup of dislocation loops, loop growth, and formation of dislocation segments observed in T91, 9CrODS maintained overall microstructure stability with much less black-dot dislocation loops. Rate theory calculations found that compared to dislocations ($\sim 10^{14} \text{ m}^{-2}$) and GBs, the high-density ($\sim 10^{23} \text{ m}^{-3}$) nanoparticles in ODS steels are much more efficient in removing point defects and suppressing the buildup of defect clusters. The RED of the 9CrODS steel enters the sink-limited regime above $\sim 150 \text{ }^\circ\text{C}$, and is greatly suppressed compared to that of the non-ODS F/M steel T91.

Acknowledgements

The authors would like to thank IVEM staff Pete Baldo and Edward Ryan at Argonne National Laboratory for their assistance with the irradiation experiments. Xiang Liu would also like to thank Professor Pascal Bellon at the University of Illinois at Urbana-Champaign for his instructions in rate theory calculations. This work was funded by the DOE Office of Nuclear Energy's Nuclear Energy University Programs (NEUP) under Contract No. DE-NE0008291. The in situ ion irradiation was accomplished at Argonne National Laboratory at the IVEM-Tandem Facility, a U.S. Department of Energy Facility funded by the DOE Office of Nuclear Energy, operated under Contract No. DE-AC02-06CH11357 by UChicago Argonne, LLC and the DOE Office of Nuclear Energy under DOE Idaho Operations Office Contract DE-AC07-051D14517 as part of a Nuclear Science User Facilities experiment.

References

- [1] G.R. Odette, M.J. Alinger, B.D. Wirth, *Annu. Rev. Mater. Res.* 38 (2008) 471–503.
- [2] G. Zhang, Z. Zhou, K. Mo, P. Wang, Y. Miao, S. Li, M. Wang, X. Liu, M. Gong, J. Almer, J.F. Stubbins, *J. Alloys Compd.* 648 (2015) 223–228.
- [3] K.A. Unocic, B.A. Pint, D.T. Hoelzer, *J. Mater. Sci.* 51 (2016) 9190–9206.
- [4] Y. Miao, K. Mo, Z. Zhou, X. Liu, K.-C. Lan, G. Zhang, M.K. Miller, K.A. Powers, J.F. Stubbins, *J. Nucl. Mater.* 480 (2016) 195–201.
- [5] M.K. Miller, D.T. Hoelzer, E.A. Kenik, K.F. Russell, *Intermetallics* 13 (2005) 387–392.
- [6] E. Aydogan, N. Almirall, G.R. Odette, S.A. Maloy, O. Anderoglu, L. Shao, J.G. Gigax, L. Price, D. Chen, T. Chen, F.A. Garner, Y. Wu, P. Wells, J.J. Lewandowski, D.T. Hoelzer, *J. Nucl. Mater.* 486 (2017) 86–95.
- [7] N.A. Bailey, E. Stergar, M. Toloczko, P. Hosemann, *J. Nucl. Mater.* 459 (2015) 225–234.
- [8] A. Certain, S. Kuchibhatla, V. Shutthanandan, D.T. Hoelzer, T.R. Allen, *J. Nucl. Mater.* 434 (2013) 311–321.
- [9] T. Chen, J.G. Gigax, L. Price, D. Chen, S. Ukai, E. Aydogan, S.A. Maloy, F.A. Garner, L. Shao, *Acta Mater.* 116 (2016) 29–42.
- [10] M.K. Miller, D.T. Hoelzer, *J. Nucl. Mater.* 418 (2011) 307–310.
- [11] J. Ribis, S. Lozano-Perez, *J. Nucl. Mater.* 444 (2014) 314–322.
- [12] X. Liu, Y. Miao, Y. Wu, S.A. Maloy, J.F. Stubbins, *Scr. Mater.* 138 (2017) 57–61.

- [13] L.L. Hsiung, M.J. Fluss, S.J. Tumej, B.W. Choi, Y. Serruys, F. Willaime, A. Kimura, *Phys. Rev. B - Condens. Matter Mater. Phys.* 82 (2010) 1–13.
- [14] O. Anderoglu, T.S. Byun, M. Toloczko, S.A. Maloy, *Metall. Mater. Trans. A* 44 (2013) 70–83.
- [15] X. Liu, Y. Miao, M. Li, M.K. Kirk, S.A. Maloy, J.F. Stubbins, *J. Nucl. Mater.* 490 (2017) 305–316.
- [16] J.F. Ziegler, M.D. Ziegler, J.P. Biersack, *Nucl. Instruments Methods Phys. Res. Sect. B Beam Interact. with Mater. Atoms* 268 (2010) 1818–1823.
- [17] R.E. Stoller, M.B. Toloczko, G.S. Was, A.G. Certain, S. Dwaraknath, F.A. Garner, *Nucl. Instruments Methods Phys. Res. Sect. B Beam Interact. with Mater. Atoms* 310 (2013) 75–80.
- [18] R. Sizmann, *J. Nucl. Mater.* 69–70 (1978) 386–412.
- [19] G.S. WAS, *Fundamentals of Radiation Materials Science*, Springer New York, New York, NY, 2017.
- [20] K. Tai, R.S. Averback, P. Bellon, Y. Ashkenazy, B. Stumphy, *J. Nucl. Mater.* 422 (2012) 8–13.
- [21] J.P. Wharry, G.S. Was, *Acta Mater.* 65 (2014) 42–55.
- [22] E. Kuramoto, T. Tsutsumi, *J. Nucl. Mater.* 212–215 (1994) 175–178.
- [23] Z.N. Ding, C.H. Zhang, Y.T. Yang, Y. Song, A. Kimura, J. Jang, *J. Nucl. Mater.* 493 (2017) 53–61.
- [24] W.-Y. Chen, *Irradiation Damage in Neutron-Irradiated FeCr Model Alloys*, University of Illinois at Urbana-Champaign, 2014.